# Determination and localized analysis of intersatellite line of sight gravity difference: Results from the GRAIL primary mission

Shin-Chan Han [1]

[1]   The line of sight (LOS) gravity difference between two coorbiting spacecrafts is determined in terms of intersatellite range-acceleration measurements available from the Gravity Recovery and Interior Laboratory (GRAIL). The precise orbit data are crucial for retrieving gravity difference from range acceleration and aligning the LOS data particularly in altitude. A relative orbit error of a few centimeters in position and a few tens μm/s in velocity is commensurate with the GRAIL-ranging instrument noise at a few μGal in LOS gravity difference. The power spectrum, as well as the topography correlation and admittance, is quantified by upward continuing the topographic potential, forward modeling the LOS gravity along the spacecraft trajectory (i.e., Bouguer correction) and comparing with the GRAIL LOS observations. Based on the data analysis from the primary GRAIL mission, I found that the LOS gravity difference observation produced near unity correlation with topography potential out to degree 550, higher than the global estimate, over the areas covered by the low-altitude orbit (~20 km). The crustal density was estimated to be 2500–2600 kg/m$^3$ with regional variations of about 10%, by minimizing the Bouguer coherence of the GRAIL data at the degree band 150–300. Systematic decrease in the density estimates by 3–4% or 100 kg/m$^3$ was observed at shorter wavelengths (degree band 300–500). It implies the inadequacy of a uniform density model across the entire lithosphere and suggests radial stratification of the bulk density (or porosity). Due to spatially localized characteristic, the LOS gravity difference data are well suited to regional analysis at the highest-possible resolution.

## 1.   Introduction

[2]   The Gravity Recovery and Interior Laboratory (GRAIL) mission aims at recovering the high-resolution global gravity fields of the Moon with unprecedented resolution and accuracy (e.g., resolution 13 km on the surface from the primary mission) [*Zuber et al.*, 2013a]. This is accomplished by precisely tracking two low-orbiting satellites with Ka-Band microwave ranging. The technical concept builds on the success of the Gravity Recovery and Climate Experiment (GRACE) mission for the Earth's static and time-variable gravity fields [*Tapley et al.*, 2004]. The fundamental observation from GRAIL is provided by the Lunar Gravity Ranging System (LGRS), which measures intersatellite distance change between two spacecrafts coorbiting around the Moon in response to the lunar gravity field. These instantaneous biased-range, range-rate, and range-acceleration data are processed by Jet Propulsion Laboratory (JPL) and are available through the Planetary Data System as Level-1B (L1B) data products. In addition to providing precision at least 1000 times better than the Earth-based tracking of lunar orbiters (like S-band or X-band Doppler), LGRS intersatellite ranging measurements are inherently more sensitive to higher-degree (shorter wavelength) gravity signals [*Zuber et al.*, 2013b].

[3]   These L1B data sets are used by JPL and Goddard Space Flight Center project teams to determine the Level-2 (L2) global gravity field using the orbit and gravity analysis software system [*Moyer*, 2005; *Pavlis et al.*, 2009; *Asmar et al.*, 2013]. The iterative computation between the orbit and the gravity field solutions is required to improve the quality of L1B science measurements [*Kruizinga et al.*, 2013]. Using the data during the primary mission, the L2 GRAIL gravity field has been developed to degree 420, corresponding to a resolution of 13 km [*Zuber et al.*, 2013a]. However, the higher-degree terms (greater than 350) are biased by noise and incomplete sampling between adjacent orbital tracks, as indicated by the Bouguer power spectrum and correlation with topography [*Wieczorek et al.*, 2013a]. More importantly, the low-orbit data, amounting ~30% of 90 days of the primary mission data and sensitive to

---

[1]Planetary Geodynamics Laboratory, NASA Goddard Space Flight Center, Greenbelt, Maryland, USA.

Corresponding author: S.-C. Han, Planetary Geodynamics Laboratory, Code 698, NASA Goddard Space Flight Center, Greenbelt, MD 20771 USA. (shin-chan.han@nasa.gov)

$$g_{LOS} = (\mathbf{g}_1 - \mathbf{g}_2)^T \mathbf{e}_{12} \text{ ... LOS gravity difference}$$
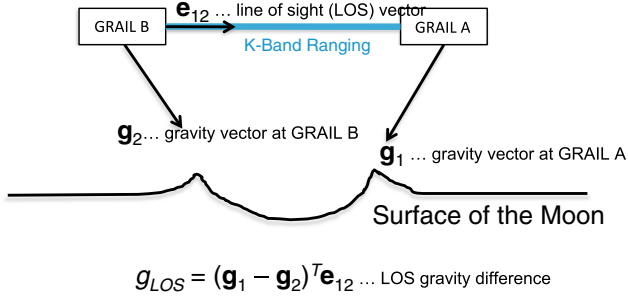
**Figure 1.** A schematic description of intersatellite LOS gravity difference.

degree ~660, were not optimally utilized by imposing a power law (smoothing) constraint and truncating the expansion degree to 420. Even for the latest development of the gravity model to degree 660 from the primary mission data [*Konopliv et al.*, 2013; *Lemoine et al.*, 2013], the low-orbit data are down weighted due to the applied power constraint that is mandatory for global expansion of the gravity field. For example, the undesired smoothing effects are discussed by *Han et al.* [2009] using the Lunar Prospector gravity models.

[4] It is possible to enhance gravity information by reanalyzing GRAIL L1B data for local areas, possibly out to degree 660 (8 km resolution) from the primary mission. For example, *Goossens et al.* [2005] demonstrated the localized analysis of the Lunar Prospector tracking data using the Doppler velocity. *Han* [2008] and *Han et al.* [2011] obtained the nearside gravity field models with substantially improved resolution to degree 200 from the Lunar Prospector extended mission by using the line of sight (LOS) Doppler acceleration data. The LOS acceleration data set from the Earth-based Doppler tracking has been used to infer high-frequency gravity signatures; a few examples include *Kaula* [1996] and *Barriot et al.* [1998] for Venus from Magellan spacecraft; *McKenzie et al.* [2002], *Beuthe et al.* [2006, 2012], and *Williams et al.* [2008] for Mars from Mars Reconnaissance Orbiter and Mars Express; *Sugano and Heki* [2004], *Han* [2008], and *Han et al.* [2011] for the Moon from Lunar Prospector. *McKenzie and Nimmo* [1997] and *Crossby and McKenzie* [2005] developed the gravity-topography admittance directly from the LOS acceleration data.

[5] The L1B intersatellite range-rate and range-acceleration data have been analyzed directly to map the Earth's gravity fields from the GRACE data. *Rowlands et al.* [2005], *Mayer-Gürr et al.* [2006], and *Han et al.* [2008] demonstrated the advantage of using short-arc integration for the regional time-variable gravity fields. Several authors exploited the energy integral to derive the gravitational potential difference from the range-rate data [*Wolff*, 1969; *Jekeli*, 1999; *Han et al.*, 2006; *Ramillien et al.*, 2011]. The range-acceleration data were used to derive the gravity difference and applied to obtain the ocean tidal gravity variation by *Killett et al.* [2011]. Both data types (range rate and range acceleration) are in principle identical and indeed derived from the biased-range measurement [*Kim*, 2000; *Kruizinga et al.*, 2013]. However, with spatial differentiation, the high-frequency gravity signals are accentuated in range acceleration.

[6] In this study, I develop a rigorous model of intersatellite LOS gravity difference in terms of range acceleration for high-frequency GRAIL gravity analysis. The LOS gravity difference

is related linearly to the gravity field and may be used for local gravity analysis by taking full advantage of low-orbit data. I discuss below the detailed algorithm used to derive the LOS gravity difference from satellite-to-satellite tracking measurements, examine various error sources including the orbit error in the LOS modeling, and present the results from the actual primary mission L1B data. I introduce a method to quantify the power and topography-correlation spectra of the GRAIL data by forward modeling the topographic potential (i.e., Bouguer) effect along the orbit and comparing with the GRAIL LOS gravity difference observations. Finally, I report the result of estimation for the bulk crustal density directly from LOS gravity difference and topography data. The spatial variation of the crustal density estimates over the globe is presented, and the estimates at two different spectral bands are discussed. A novel aspect of this approach is that it exploits the L1B data to directly constrain geophysical models at the highest-possible resolution over various areas, further expanding the science return from the GRAIL mission.

## 2. Observation of Intersatellite LOS Gravity Difference

[7] In this section, I derive the gravity difference along the LOS direction between two satellites using intersatellite ranging measurements. Figure 1 is a schematic of the LOS component of in situ gravity vector difference. The lunar gravity field influences two GRAIL satellites differently from their distinct locations. If the gravity exerted on GRAIL A and B satellites are $\mathbf{g}_1$ and $\mathbf{g}_2$, respectively, then their difference $\mathbf{g}_{12} = \mathbf{g}_1 - \mathbf{g}_2$ is generally a few 100 mGal ($10^{-5}$ m/s$^2$) at 50 km altitude. The LOS gravity difference $g_{LOS}$ is then defined as gravity difference "vector" $\mathbf{g}_{12}$ projected along the LOS direction $\mathbf{e}_{12}$ between two satellites (i.e., $g_{LOS} \equiv \mathbf{g}_{12} \cdot \mathbf{e}_{12}$).

[8] The LOS gravity difference $g_{LOS}$ is in situ measurement of the lunar gravity field at the satellite altitude. It is directly related to the gravity field of the planet in contrast to the ranging (positional) measurement involving numerical integration of gravitational potential. However, it is important to distinguish the LOS gravity difference from range acceleration that is immediately available from the LGRS measurement. I derive a LOS gravity observation model by highlighting the distinction between it and range acceleration, as well as discussing the possible modeling errors induced by errors in the orbit.

[9] I start with the satellite-to-satellite tracking observation model developed originally for the GRACE mission [*Kim*, 2000]. The instantaneous range between two satellites such as GRAIL, $\rho$, can be expressed with the relative position vector $\mathbf{x}_{12}$:

$$\rho = \mathbf{x}_{12} \cdot \mathbf{e}_{12}, \tag{1}$$

where the LOS unit vector is $\mathbf{e}_{12} = \mathbf{x}_{12}/\rho$. The range rate is given by

$$\dot{\rho} = \dot{\mathbf{x}}_{12} \cdot \mathbf{e}_{12}. \tag{2}$$

[10] This is from the mutual orthogonality of a unit vector and its time derivative ($\mathbf{e}_{12} \cdot \mathbf{e}_{12} = 1$ and thus $\mathbf{e}_{12} \cdot \dot{\mathbf{e}}_{12} = 0$), where $\dot{\mathbf{e}}_{12} = (\dot{\mathbf{x}}_{12} - \dot{\rho}\mathbf{e}_{12})/\rho$. Then, the range acceleration is

$$\ddot{\rho} = \ddot{\mathbf{x}}_{12} \cdot \mathbf{e}_{12} + \dot{\mathbf{x}}_{12} \cdot \dot{\mathbf{e}}_{12}, \tag{3}$$

where $\ddot{\mathbf{x}}_{12}$ is the kinematic acceleration difference between

two satellites that include the gravitational acceleration difference $\mathbf{g}_{12}$ and nonconservative force difference $\mathbf{f}_{12}$ ($\ddot{\mathbf{x}}_{12} = \mathbf{g}_{12} + \mathbf{f}_{12}$). The last term of the right-hand side $\dot{\mathbf{x}}_{12} \cdot \dot{\mathbf{e}}_{12}$ differentiates LOS gravity difference $\mathbf{g}_{12} \cdot \mathbf{e}_{12}$ from range acceleration $\ddot{\rho}$.

[11] Equation (3) indicates that one obtains the unknown gravity difference $\mathbf{g}_{12}$ along the spacecrafts by measuring range acceleration $\ddot{\rho}$ and computing the relative satellite orbit $\mathbf{x}_{12}$ and $\dot{\mathbf{x}}_{12}$ (assuming that the nonconservative force is sufficiently well modeled). The range acceleration can be used directly for gravity analysis once the orbits are given to the commensurate accuracy for computing $\dot{\mathbf{x}}_{12} \cdot \dot{\mathbf{e}}_{12}$. The actual orbit is different from the computed one. To examine such orbit error effect, I introduce the errors in the relative orbit: $\mathbf{x}_{12} = \tilde{\mathbf{x}}_{12} + \delta\mathbf{x}_{12}$ and $\dot{\mathbf{x}}_{12} = \tilde{\dot{\mathbf{x}}}_{12} + \delta\dot{\mathbf{x}}_{12}$ (or, equivalently, in terms of the LOS unit vector, $\mathbf{e}_{12} = \tilde{\mathbf{e}}_{12} + \delta\mathbf{e}_{12}$ and $\dot{\mathbf{e}}_{12} = \tilde{\dot{\mathbf{e}}}_{12} + \delta\dot{\mathbf{e}}_{12}$), where the parameters with tilde on the top of the variables indicate the computed (or measured) quantities using the orbit data and the ones with delta imply the associated errors. Note that only the relative (not absolute) orbit error matters at this moment. Introducing them into equation (3), I obtain

$$\ddot{\rho} = \mathbf{g}_{12} \cdot \tilde{\mathbf{e}}_{12} + \mathbf{f}_{12} \cdot \tilde{\mathbf{e}}_{12} + \tilde{\dot{\mathbf{x}}}_{12} \cdot \tilde{\dot{\mathbf{e}}}_{12}$$
$$+ \left( \tilde{\mathbf{g}}_{12} \cdot \delta\mathbf{e}_{12} + \tilde{\dot{\mathbf{x}}}_{12} \cdot \delta\dot{\mathbf{e}}_{12} + \delta\dot{\mathbf{x}}_{12} \cdot \tilde{\dot{\mathbf{e}}}_{12} \right). \quad (4)$$

[12] In equation (4), I disregarded the second-order term $\delta\dot{\mathbf{x}}_{12} \cdot \delta\dot{\mathbf{e}}_{12}$. The nonconservative force term $\mathbf{f}_{12}$ is in general within 1 $\mu$Gal; however, it could be 10 times larger for a short period when one of the GRAIL satellites is in shadow and the other is not (computed along the orbit at 50 km altitude using the GEODYN software [*Pavlis et al.*, 2009]). Therefore, the quantity $\mathbf{f}_{12} \cdot \delta\mathbf{e}_{12}$ is negligible and omitted in equation (4). The error term $\mathbf{g}_{12} \cdot \delta\mathbf{e}_{12}$ is approximated to $\tilde{\mathbf{g}}_{12} \cdot \delta\mathbf{e}_{12}$, where $\tilde{\mathbf{g}}_{12}$ is computed gravity difference vector from the a priori gravity model. By rearranging equation (4), I have

$$\ddot{\rho} - \mathbf{f}_{12} \cdot \tilde{\mathbf{e}}_{12} - \tilde{\dot{\mathbf{x}}}_{12} \cdot \tilde{\dot{\mathbf{e}}}_{12} = \mathbf{g}_{12} \cdot \tilde{\mathbf{e}}_{12} + \Delta, \quad (5)$$

where the entire left-hand side can be obtained from L1B data, the term $\mathbf{g}_{12} \cdot \tilde{\mathbf{e}}_{12}$ of the right-hand side is (unknown) instantaneous LOS gravity difference, and its modeling error $\Delta$ is explicitly given by

$$\Delta = (\tilde{\mathbf{g}}_{12}) \cdot \delta\mathbf{e}_{12} + (\tilde{\dot{\mathbf{e}}}_{12}) \cdot \delta\dot{\mathbf{x}}_{12} + (\tilde{\dot{\mathbf{x}}}_{12}) \cdot \delta\dot{\mathbf{e}}_{12}. \quad (6)$$

[13] I individually examine three error terms of $\Delta$ representing the LOS gravity modeling error due to errors in the relative orbital state vectors, $\delta\mathbf{x}_{12}$ and $\delta\dot{\mathbf{x}}_{12}$. The upper bound of each error is derived in the Appendix A. When the magnitude of relative position error $|\delta\mathbf{x}_{12}|$ and relative velocity error $|\delta\dot{\mathbf{x}}_{12}|$ is given in m and m/s, respectively, three LOS modeling error terms in m/s$^2$ are bounded by

$$(\tilde{\mathbf{g}}_{12}) \cdot \delta\mathbf{e}_{12} < 10^{-6} |\delta\mathbf{x}_{12}|, \quad (7a)$$

$$(\tilde{\dot{\mathbf{e}}}_{12}) \cdot \delta\dot{\mathbf{x}}_{12} < 10^{-3} |\delta\dot{\mathbf{x}}_{12}|, \quad (7b)$$

$$(\tilde{\dot{\mathbf{x}}}_{12}) \cdot \delta\dot{\mathbf{e}}_{12} < 1 \times 10^{-6} |\delta\mathbf{x}_{12}| + 2 \times 10^{-3} |\delta\dot{\mathbf{x}}_{12}| \text{ m/s}^2. \quad (7c)$$

[14] They imply that the relative orbit data with the accuracy of centimeters and 10 $\mu$m/s cause the maximum error in $\mu$Gal for LOS gravity difference. The accuracy of the

GRAIL satellite orbit (such as from Planetary Data System (PDS) and NASA's Navigation and Ancillary Information Facility (NAIF)/SPICE) is a few centimeters in terms of intersatellite range error (a proxy of relative position accuracy) and 20 $\mu$m/s in terms of range-rate error (a proxy of relative velocity accuracy) [*Kruizinga et al.*, 2013]. The orbit error is dominant at one cycle-per-revolution (1 cpr) frequency corresponding to the central or degree-zero gravity term (a point mass gravity term; $GM/a^2$); however, it becomes 2 orders of magnitude smaller beyond the 1 cpr frequency; therefore, the absolute magnitude of $\Delta$ should be much smaller at the bandwidth higher than 1 cpr ($> 0.15$ mHz) that is of interest.

[15] There is another error source, which is implicit and caused by misalignment of the LOS gravity data along the orbit. In equation (5), $\mathbf{g}_{12}$ is evaluated along the actual (unknown) trajectory. However, access to the gravity is only along the computed trajectory. Such misalignment error in the LOS gravity difference can be expressed as

$$\acute{\Delta} = \acute{\mathbf{g}}_{12} \cdot \tilde{\mathbf{e}}_{12} - \mathbf{g}_{12} \cdot \tilde{\mathbf{e}}_{12}, \quad (8)$$

where $\mathbf{g}_{12} = \mathbf{g}_{12}(\mathbf{r})$ is the actual (unknown) gravity difference vector along the actual (unknown) trajectory $\mathbf{r}$. $\acute{\mathbf{g}}_{12} = \mathbf{g}_{12}(\tilde{\mathbf{r}})$ is the actual (unknown) gravity difference vector along the calculated trajectory $\tilde{\mathbf{r}}$.

[16] Encompassing these error sources in equations (6) and (8) and measurement noise, the LOS observational model is rewritten as follows:

$$g_{\text{LOS}} = \tilde{\ddot{\rho}} - \tilde{\dot{\mathbf{x}}}_{12} \cdot \tilde{\dot{\mathbf{e}}}_{12} + \mathbf{t}_{12} \cdot \tilde{\mathbf{e}}_{12} - \mathbf{f}_{12} \cdot \tilde{\mathbf{e}}_{1212} - \Delta + \acute{\Delta} + \varepsilon, \quad (9)$$

where $g_{\text{LOS}} = \acute{\mathbf{g}}_{12} \cdot \tilde{\mathbf{e}}_{12}$. Note that access is only provided to $\mathbf{g}'_{12}$ but not to $\mathbf{g}_{12}$. $\ddot{\rho}$ is the range-acceleration measurement from LGRS, and $\varepsilon$ is its instrumental noise. In this final form, I separate the term $\mathbf{t}_{12}$ (time-variable gravitational acceleration difference such as tide and planetary bodies' attraction) from $\mathbf{g}_{12}$, so that $g_{\text{LOS}}$ represents only the static gravity field. The modeling errors of $\mathbf{t}_{12}$ and $\mathbf{f}_{12}$ are assumed to be negligible for this study. The dynamic range of $g_{\text{LOS}}$ is computed to be 200, 40, and 1 mGal for degrees from 2, 120, and 400, respectively, from the topographic potential model. It is a factor $10^3$–$10^5$ greater than the maximum of $\Delta$ ($\sim\mu$Gal) attainable with the present orbit data. The instrument noise $\varepsilon$ (to be shown in section 4) is a few times greater than $\Delta$. I thus neglect the LOS modeling error $\Delta$.

[17] With this, equation (9) indicates that the instantaneous LOS gravity difference between two GRAIL satellites $g_{\text{LOS}}$ can be obtained from L1B range-acceleration and orbit data, and time-variable and nongravity acceleration models with the error limited mostly by LGRS instrumental noise $\varepsilon$ and also by the misalignment error $\Delta'$. In section 4, I quantify $\Delta'$ numerically by various simulations and $\varepsilon$ from the actual measurement. I also quantify each "signal" terms of $\tilde{\ddot{\rho}}$, $\tilde{\dot{\mathbf{x}}}_{12} \cdot \tilde{\dot{\mathbf{e}}}_{12}$, $\mathbf{t}_{12} \cdot \tilde{\mathbf{e}}_{12}$, and $\mathbf{f}_{12} \cdot \tilde{\mathbf{e}}_{1212}$ and compare them with the error term of $\Delta'$ and $\varepsilon$.

## 3. Modeling of Intersatellite LOS Gravity Difference from Topography

[18] The gravity effect of surface topography (i.e., Bouguer correction) can be computed in terms of LOS gravity difference along the orbit. First, I use the global topography coefficients such as from Lunar Orbiter Laser Altimeter (LOLA)
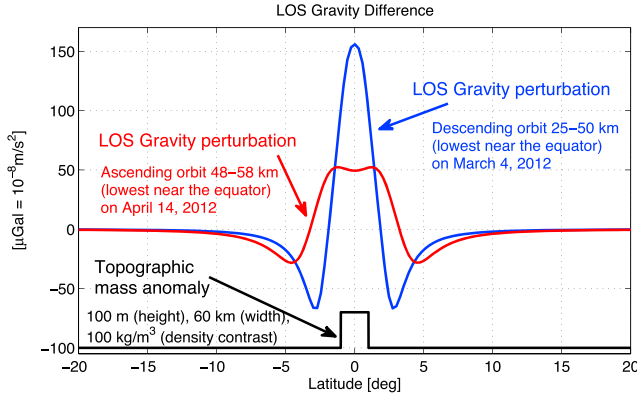
**Figure 2.** An example of synthetic LOS gravity difference, evaluated along the GRAIL orbits at 25–60 km, generated by a topographic mass anomaly at the equator. The mass anomaly has a dimension of $2° \times 2°$ ($\sim 60$ km $\times$ 60 km) and 0.1 km in height with 100 kg/m$^3$ of density contrast. It yields the LOS gravity difference of 150–50 μGal at 25–50 km altitude. The GRAIL measurement accuracy in LOS gravity difference is a few μGal at 0.1 Hz.

data [*Smith et al.*, 2010] but referenced in the principal axis coordinate system. These coefficients are available from PDS Geosciences Node (http://pds-geosciences.wustl.edu/lro/lro-l-lola-3-rdr-v1/lrolol_1xxx/data/lola_shadr/pa/). The gravitational potential coefficients are computed from the topography coefficients using the method given by *Wieczorek and Phillips* [1998] considering finite amplitude of topography rather than condensed mass on the surface. Following the notation in *Wieczorek and Phillips* [1998], they are

$$C_{ilm}^+ = \gamma T_{ilm}, \tag{10a}$$

$$T_{ilm} = \left(\frac{D}{a}\right)^l \frac{4\pi D^3}{M(2l+1)} \sum_{n=1}^{l+3} \frac{{}^n h_{ilm}}{D^n} \frac{\Pi_{j=1}^n(l+4-j)}{n!(l+3)}, \tag{10b}$$

where $C_{ilm}^+$ is a dimensionless gravitational potential coefficient referenced to a radius $a$, $\gamma$ is a nominal crustal density used to compute gravitational attraction by surface topography, $D$ is the mean spherical radius of the topography, and ${}^n h_{ilm}$ is the spherical harmonic coefficient of the topography raised by the $n$th power (e.g., equation (8) of *Wieczorek and Phillips* [1998]). For GRAIL's sensitivity to higher-degree gravity signals, the finite amplitude expansion is considered up to order $n = 9$ in this study.

[19] The Bouguer correction in terms of LOS gravity difference can be expressed in terms of spherical harmonic series with two given positions of satellites as follows:

$$g_{LOS}^B(\gamma) = \gamma p_{LOS}, \tag{11a}$$

$$p_{LOS} = \tilde{\mathbf{e}}_{12} \cdot \mathbf{T}_{12}(\theta_1, \lambda_1, r_1, \theta_2, \lambda_2, r_2), \tag{11b}$$

$$\mathbf{T}_{12}(\theta_1, \lambda_1, r_1, \theta_2, \lambda_2, r_2) = \frac{GM}{a} \sum_{l=2}^{L} \sum_{m=0}^{l} \sum_{i=1}^{2} T_{ilm}$$

$$\left[ \nabla \left\{ \left(\frac{a}{r_1}\right)^{l+1} Y_{ilm}(\theta_1, \lambda_1) \right\} - \nabla \left\{ \left(\frac{a}{r_2}\right)^{l+1} Y_{ilm}(\theta_2, \lambda_2) \right\} \right], \tag{11c}$$

where $GM$ is the gravitational constant times mass of the Moon and $\tilde{\mathbf{e}}_{12}$ is a LOS unit vector between two locations at $(\theta_1, \lambda_1, r_1)$ and $(\theta_2, \lambda_2, r_2)$ that are two sets of spherical coordinates of the spacecrafts and $Y_{ilm}$ is the (surface) spherical harmonic functions as in *Wieczorek and Phillips* [1998]. $L$ is the maximum degree of spherical harmonic expansion of $g_{LOS}^B$. Equations (11a)–(11c) indicate that one evaluates the gravity vectors at two spacecrafts' locations through the gradient operator $\nabla$ and projects their difference onto the LOS direction. It can be computed as time series along the trajectory of spacecrafts. It is worth to mention that the variable $p_{LOS}$ is completely determined from the topography and orbit data, and the Bouguer correction $g_{LOS}^B(\gamma)$ is linearly proportional to the (unknown) density $\gamma$. Therefore, it is possible to estimate the density parameter directly by comparing the time series of the GRAIL measurements $g_{LOS}$ and the topography synthetics $p_{LOS}$.
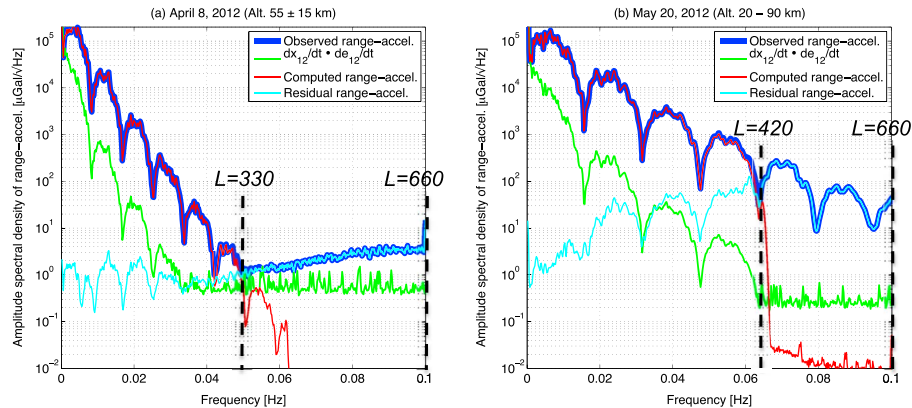


**Figure 3.** Square root of power spectral density (PSD) of L1B range-acceleration measurement (thick blue), of the computed range acceleration from L1B orbit (red), of the orbital correction term $\tilde{\mathbf{x}}_{12} \cdot \tilde{\mathbf{e}}_{12}$ (green), and of the residual (observed minus computed) range acceleration (cyan). The observational noise is in a few μGal in range acceleration at a 5 s sampling (0.1 Hz). Shown are the 1 day L1B data on 8 April 2012 with relatively circular orbits at average altitude of 55 km and on 20 May 2012 with altitudes varying from 20 to 90 km. The spherical harmonic degree $L$ is computed by $L \approx 6623\, f$, where $f$ is frequency. The spatial resolution is obtained by 5600 km/$L$.
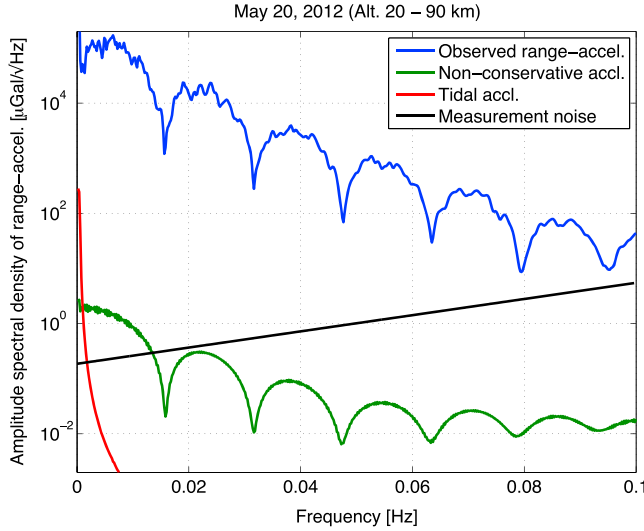
May 20, 2012 (Alt. 20 – 90 km)

**Figure 4.** Same as Figure 3, but it shows nongravitational force (green) and time-variable tidal acceleration (red) for comparison with the range-acceleration measurement (blue) and the measurement noise (black). The PSD of measurement noise is computed by fitting a simple function scaling with frequency to the actual measurement PSD on 8 April 2012 over the frequency band where the noise is dominant (i.e., $L = 320$–$660$).

[20] For demonstration purposes, I computed a LOS gravity difference caused by a synthetic mass anomaly on the equator and evaluated along two GRAIL orbits at different altitudes: the one along the descending orbit with altitudes from 25 to 50 km was lowest near the equator on 4 March 2012 and the other along the ascending orbit with altitudes 48 to 58 km on 14 April 2012. The mass anomaly specified had a dimension of $2° \times 2°$ (60 km $\times$ 60 km) and 0.1 km in height and a 100 kg/m$^3$ density contrast. The model yielded a LOS gravity difference of 150 and 50 µGal at 25 km and 50 km altitude, respectively (Figure 2). A fractured rock with 3% porosity and 100 m thickness over a 60 km area is well above the detectable range from GRAIL L1B data because the GRAIL LGRS has measurement noise of a few µGal at 5 s sampling (section 4 and Figures 3 and 4). As can be seen from Figure 2, the gravitational effect of such mass anomaly in LOS gravity difference is more localized with larger amplitude at lower altitude.

## 4. Analysis of L1B Data

[21] During the 90 day (March to May 2012) science phase of the primary mission, the GRAIL spacecrafts were orbiting with a wide range of variation in altitude from 20 to 90 km (relative to a sphere with a radius of 1737.4 km). From the second half of March to early May, the altitude was about $55 \pm 15$ km in relatively circular orbits. The orbit was rather elliptical during the rest of period, with periapsis and apoapsis ~20 and ~90 km, respectively [*Zuber et al.*, 2013a]. The nominal L1B data with altitude variation of $55 \pm 10$ km on 8 April 2012 and the low-orbit L1B data with altitude as low as 20 km on 20 May 2012 are compared in Figure 3. I computed the square root of power spectral density (PSD) of range acceleration for the following cases: $\tilde{\ddot{\rho}}$, observed range acceleration from LGRS

(thick blue line); $\tilde{\mathbf{x}}_{12} \cdot \tilde{\mathbf{e}}_{12}$, orbital correction term (green line); $d\left(\tilde{\mathbf{x}}_{12} \cdot \tilde{\mathbf{e}}_{12}\right)/dt$, computed range acceleration from the L1B orbit data (red line); $\tilde{\ddot{\rho}} - d\left(\tilde{\mathbf{x}}_{12} \cdot \tilde{\mathbf{e}}_{12}\right)/dt$, residual range acceleration (cyan line).

[22] The power spectrum of each time series data for both days was estimated using the Welch's periodogram method [*Welch*, 1967] with the window width of 5120 s that includes total 1024 samples of the 5 s data.

[23] As discussed in equation (15) of *McKenzie and Nimmo* [1997], the frequency $f$ in the time domain is related to the wavelength $\lambda$ in the space domain through $f = v/\lambda$ where $v$ is the orbital speed. As a rule of thumb, the spherical harmonic degree $L$ corresponding to the wavelength $\lambda$ is given by $L = 2\pi r/\lambda$, where $r$ is the radius of the orbit. Therefore, one can obtain the spherical harmonic degree $L$ from the temporal frequency $f$ through

$$L = \frac{2\pi (a + h)}{v} f, \tag{12}$$

where $a$ is mean radius of the Moon (1737.4 km), $h$ is average altitude of satellites (55 km), and $v$ is average speed of satellites (1.7 km/s). It gives $L \approx 6623 f$ when $f$ is given in hertz. For the rather elliptical orbit with 20–90 km altitude variation, it is variable from $L \approx 6534 f$ to $L \approx 7088 f$. In this study, I use $L \approx 6623 f$ to approximately obtain the spherical harmonic degree $L$ from the time domain spectra.

[24] In Figure 3, it is apparent from the nominal data in April that the LGRS range-acceleration observation noise overwhelms the gravitational signal starting at 50 mHz ($L = 330$). The overall LGRS instrumental noise spectrum can be deduced from this data set. The noise is around 1 µGal/√Hz around 50 mHz and grows with frequency (degree) becoming a few µGal/√Hz at 0.1 Hz ($L = 660$). On the contrary, the gravitational signals show the decreasing power with increasing frequency. The power spectrum from the data in 20 May (Figure 3b) is biased by the data acquired at low altitudes (~20 km). The magnitude of LGRS range-acceleration data from the low orbit is considerably larger than the nominal one. In this case, the gravitational signal in the LGRS data is larger than the instrumental noise over all frequencies up to the Nyquist frequency of 0.1 Hz ($L = 660$).

[25] I computed the range acceleration using the orbital state vector data available as a part of L1B data set. As indicated in the data description, the gravity field model used for computing these orbits is an internal JPL field, 420b8a, expanded to degree 420, an earlier version of the field used in *Zuber et al.* [2013a]. The abrupt drop in power from the synthetic range acceleration at 64 mHz ($L = 420$) is evident in Figure 3 (red lines). In addition, there is a minute degradation of the power in the synthetic range acceleration starting around 58 mHz ($L = 380$) in Figure 3b. This might indicate the dampening effect of the power law constraint applied to stabilize high-degree components for the field 420b8a. The power spectrum of the residual range acceleration (i.e., observed minus calculated, depicted with cyan line) is not much different from the instrumental noise for the case of the nominal orbit (Figure 3a), while it is considerably larger for the case of low orbit over the entire spectral band (Figure 3b). It implies that there is considerable remaining gravity information not modeled in the field 420b8a, not only beyond 420 but also below 420.
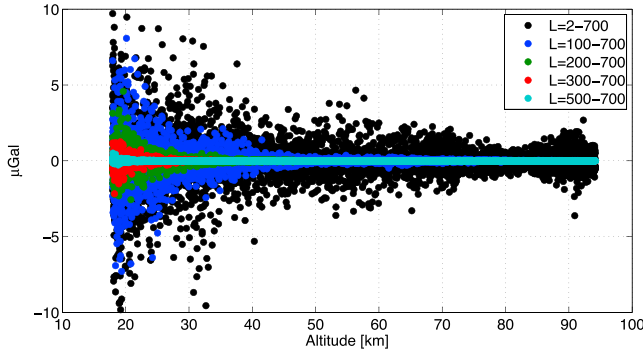
**Figure 5.** The misalignment error of the LOS gravity difference observation due to the noisy position data. The simulation was performed assuming 1 m random error in each coordinate of two spacecrafts. The error was depicted with various degree bands and altitudes.

[26] To obtain the gravitational signal, one needs to subtract $\tilde{\mathbf{x}}_{12} \cdot \tilde{\mathbf{e}}_{12}$ from the range acceleration as shown in equation (9). In Figure 3, the correction of $\tilde{\mathbf{x}}_{12} \cdot \tilde{\mathbf{e}}_{12}$ (green line) is about 2 orders of magnitude smaller than the range acceleration consistently over the entire frequency but larger than the instrumental noise particularly at the frequency below 50–60 mHz ($L = 300$–$400$). Without $\tilde{\mathbf{x}}_{12} \cdot \tilde{\mathbf{e}}_{12}$, the range-acceleration data differ from the gravity field with the error of several percentages of the gravity signal at each frequency. For the frequency higher than 70 mHz ($L = 450$), the measurement noise becomes larger and thus the correction of $\tilde{\mathbf{x}}_{12} \cdot \tilde{\mathbf{e}}_{12}$ becomes less important, i.e., the range acceleration itself could be representative of the LOS gravity difference. Therefore, when the low-altitude data (such as from the extended mission) are analyzed for the higher-degree gravity field with respect to the gravity model from the primary mission, the residual range acceleration itself could be interpreted as the residual gravity difference without such orbital correction.

[27] The other corrections of nonconservative acceleration $\mathbf{f}_{12} \cdot \tilde{\mathbf{e}}_{12}$ (mostly solar and planetary radiation pressure for the Moon) and of time-varying gravitational acceleration $\mathbf{t}_{12} \cdot \tilde{\mathbf{e}}_{12}$ (such as tides) are computed and shown in Figure 4. The instrumental noise spectrum was determined in the form of $10^{af+b}$ where $f$ is frequency and two constants $a$ and $b$ were found by fitting the function to the PSD of the nominal primary mission data on 8 April 2012 (Figure 3a). The lower degree noise spectrum was thus extrapolated. The time-variable term $\mathbf{t}_{12} \cdot \tilde{\mathbf{e}}_{12}$ is largely dominant at a global scale such as degree 2 while the nongravitational term $\mathbf{f}_{12} \cdot \tilde{\mathbf{e}}_{12}$ is rather spatially localized (i.e., whiter spectrum). When compared in terms of LOS gravity difference, these corrections are smaller than the instrumental noise for the higher frequency ($f > 15$ mHz or $L > 100$).

[28] I numerically quantified the misalignment error $\Delta'$ one encounters when evaluating the gravity difference along the imperfect trajectory. The random error of 1 m at each coordinate was assumed for GRAIL L1B orbits [*Kruizinga et al.*, 2013] and applied to both satellites. Using the gravitational potential computed from topography with the density of 2550 kg/m³ that may explain the global gravity field [*Wieczorek et al.*, 2013a], I computed the LOS gravity difference along the trajectory with and without the random errors

in position vectors. The misalignment error $\Delta'$ was quantified by the difference between them. It could be as large as a few µGal with random position error of 1 m, but it exponentially decreases with increasing degrees for shorter wavelengths and at higher altitudes (Figure 5). For the data at the altitude higher than 40 km, the error is 1 µGal or less. For the gravity field at higher degrees ($L > 200$), it is around a couple of µGal even at the lower altitudes (20 km). For the data below 40 km and gravity components at lower degrees ($L < 200$), the position error could be a source of major error. However, the actual orbit errors are nonrandom but highly correlated and dominant at low frequencies at 1 cpr and 2 cpr. It implies the quantification of $\Delta'$ with the random error assumption is an upper bound.

## 5. Comparison of LOS Gravity Difference With Topography

[29] I examined a half revolution (1 h) worth of the actual L1B data over the lunar farside around longitude of 117°W on 9 April 2012 (higher altitude) and on 20 May 2012 (lower
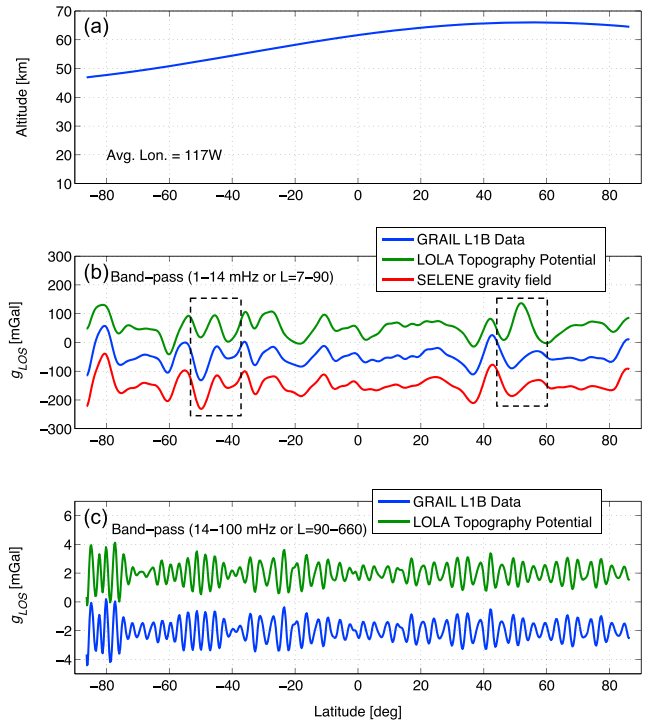


**Figure 6.** A sample of LOS gravity difference data over the farside (longitude 117°W) on 9 April 2012. One hour (half revolution) worth of the data is presented. (a) Altitude; (b) LOS gravity difference computed from SELENE gravity model and from LOLA topography potential and observed from GRAIL within the degree band from $L = 7$–$90$ (three curves were separated by 100 mGal). The large differences between gravity and topography are highlighted with dashed boxes; (c) LOS gravity difference observed from GRAIL and computed from LOLA topography within the degree band from $L = 90$–$660$ (two curves were separated by 4 mGal). The GRAIL measurement accuracy of LOS gravity difference from the 7–90 band is less than 1 µGal. The one for the 90–660 band is a few µGals.
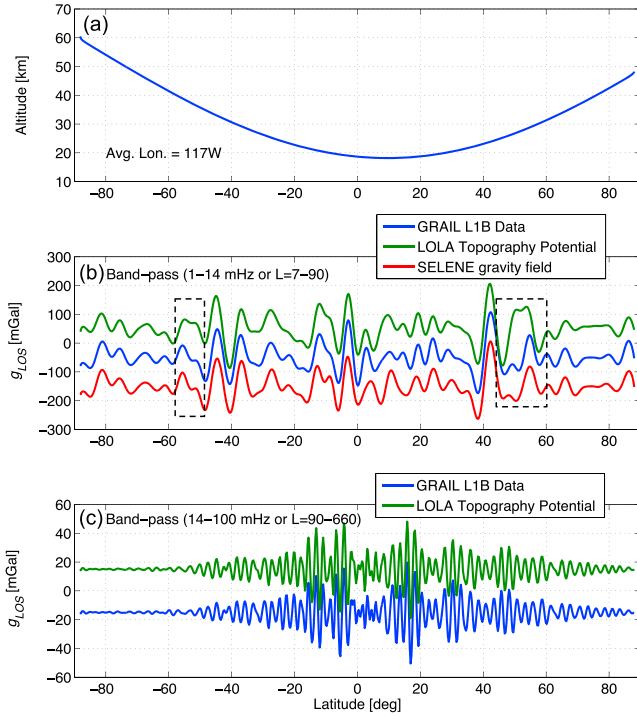
**Figure 7.** Same as Figure 6 but on 20 May 2012 with lower altitudes. The curves in Figure 7c were separated by 100 mGal and the ones in the bottom by 30 mGal.

altitude). Figure 6a shows the average altitude variation of two GRAIL satellites from south to north. The L1B Ka-Band Ranging (KBR) range-acceleration data were processed to obtain LOS gravity difference data; these data were band-pass filtered to highlight the signals from degrees 7 to 90 (1–14 mHz) and from degrees 90 to 660 (14–100 mHz). The first band was chosen for comparison with the Selenological and Engineering Explorer (SELENE) (Kaguya) gravity model while the second band is observed only from GRAIL. The time series of these two data sets (the low-degree band of 7–90 and the high-degree band of 90–660) are shown in Figures 6b and 6c, respectively. Note that the SELENE gravity model SGM150 [*Goossens et al.*, 2011] extends to degree 150, which is applicable only for the nearside with the tracking data from the Lunar Prospector (LP) extended mission [*Konopliv et al.*, 2001], and SGM150 is valid globally to degree 90 or less.

[30] For the low-degree band (7–90) shown in Figure 6b, the GRAIL LOS gravity difference data are in better agreement with the predicted signal from SGM150 (correlation coefficient of 0.997 and difference of 3 mGal) than the synthetic gravity signal from LOLA topography with the density of 2550 kg/m$^3$ (correlation coefficient of 0.624 and difference of 25 mGal). The distinction between GRAIL gravity data and LOLA topography potential model is particularly clear over the latitudes of 50°S–40°S and 50°N–60°N (marked with dashed boxes in Figure 6b). Geophysical processes, such as mascons and crustal flexure, are important at this low-degree band and may complicate a gravity response from topography [*Wieczorek et al.*, 2013a]. A few mGal of difference between GRAIL L1B and SGM150 is entirely due to error in SGM150 model, because GRAIL L1B data are as accurate as less than 1 μGal within this band. *Zuber et al.* [2013a]

shows 3–4 orders of magnitude improvement in the GRAIL gravity model over the SELENE gravity model.

[31] For the high-degree band (90–660) shown in Figure 6c, the LOS gravity difference data were compared with the LOLA topography potential model. The correlation coefficient is 0.983 and the difference is sub mGal. Such a difference may be attributed to variation of crustal density dependent on spatial locations and depths since the LOS gravity data are as accurate as several μGal at this high-degree band.

[32] Figure 7 presents the same analysis but the data from the lower altitudes on 20 May 2012. Compared to Figure 6, the signal is amplified by a factor 2–3 at the low-degree band (7–90) in Figure 7b and by 1 order of magnitude at the high-degree band (90–660) in Figure 7c. This is because the gravitational signal attenuates with altitude by a larger amount at higher degrees. For the low-degree band, GRAIL L1B data and SGM150 are agreed with a correlation coefficient of 0.951 and a difference of 13 mGal, while GRAIL data and LOLA model show a correlation coefficient of 0.841 and a difference of 29 mGal. Again, at this band, the deviation of GRAIL data from SGM150 is entirely due to errors in SGM150 while that from LOLA model is mostly due to geophysical processes causing complex gravity response from topography. For the high-degree band, the GRAIL gravity data and LOLA topography potential model are highly correlated (0.991), indicating substantial influence of surface topography in high-degree gravity components.

[33] I computed the correlation and admittance spectra between GRAIL LOS gravity data and LOLA topography directly from the one-dimensional Fourier transforms of the observed and synthetic time series data. The 6 days of GRAIL LOS gravity difference data from 12–17 April 2012 were processed. The ground tracks and altitude are shown in Figure 8a. These data were compared with the LP and SELENE gravity models and LOLA topographic potential model, in terms of square root of PSD (i.e., amplitude) in Figure 8b. Starting the frequency 15 mHz ($L = 100$), the amplitude spectra of LP and SELENE gravity models deviate from the predicted power of LOLA topographic potential and from the observed power of GRAIL L1B. The results presented here are similar to Figure 2A of *Zuber et al.* [2013a] but different in the sense that the result here represents the signals limited to the areas covered by 6 days of the orbit while the one in *Zuber et al.* [2013a] shows a global average. The LGRS measurement noise becomes apparent from 53 mHz ($L = 350$) and higher. I computed the Bouguer LOS gravity difference by subtracting the topographic effect $g_{LOS}^B(\gamma)$ with the density of 2550 kg/m$^3$ from the GRAIL observations. It corresponds to the Bouguer gravity anomaly but applied along the spacecraft trajectory by upward continuation of the topographic potential. The power spectrum of the Bouguer anomaly of LOS gravity difference, i.e., $g_{LOS} - g_{LOS}^B(\gamma)$, indicates reduction of the observed LOS gravity difference by 1 order of magnitude at frequencies higher than 10 mHz, below which the lithospheric flexure and mascon effects are most important. The Bouguer anomaly degrades from 45 mHz ($L = 300$). This indicates that the primary mission data with the nominal altitude of 55 km is sensitive to the gravity signal up to degree 300.

[34] I computed the cross-power spectrum and correlation of GRAIL LOS gravity difference observations and SELENE and
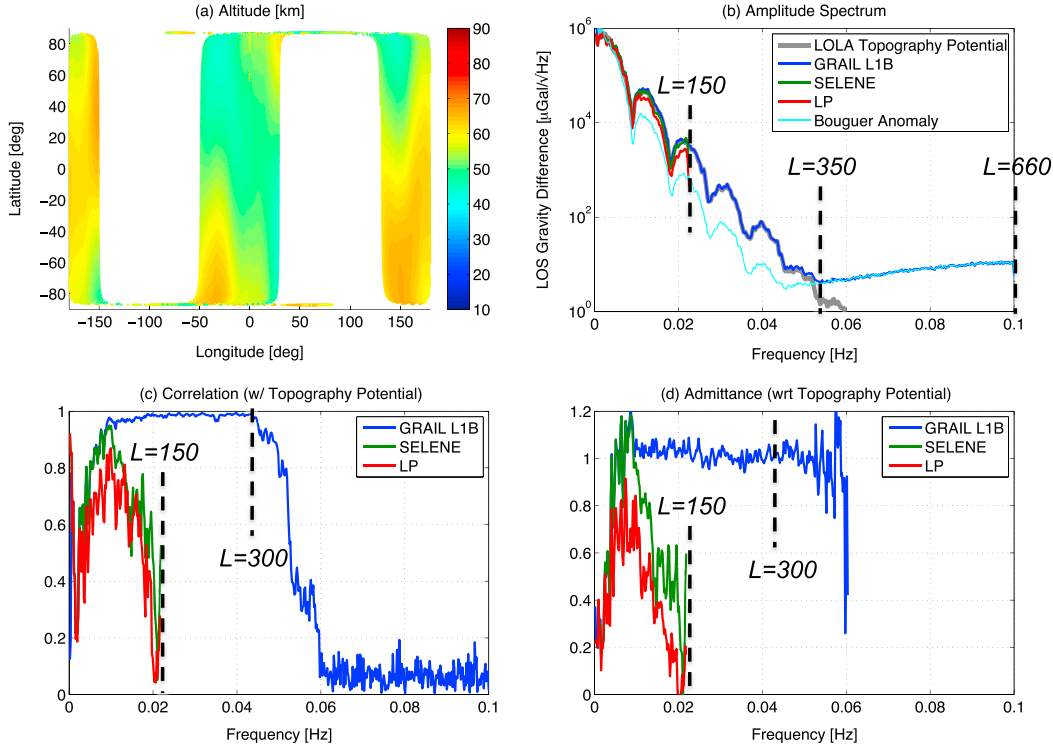
**Figure 8.** (a) The average altitude of GRAIL satellites during the period from 12 to 17 April 2012; (b) The amplitude spectrum of LOS gravity difference computed from LOLA topography, and SELENE and LP gravity models and observed from GRAIL. The Bouguer anomaly spectrum is computed by subtracting the topography effect from the observations using the nominal density of 2550 kg/m$^3$; (c) The correlation spectrum of the GRAIL observation and the synthetics from SELENE and LP gravity models with the topographic potential model; (d) The admittance spectrum of GRAIL data and SELENE and LP gravity models to the topographic potential model. Only 6 days of L1B data were used.

LP synthetics with the LOLA topographic potential model in Figure 8c. This is similar with Figure 2B of *Zuber et al.* [2013a], but, again, the result here represents the correlation over the local areas. The (local) correlation of L1B LOS gravity difference observation yields almost unity correlation to 45 mHz ($L = 300$) and drops quickly afterward. The admittance spectra of the GRAIL LOS gravity difference and SELENE and LP synthetics were computed with the topographic potential model and shown in Figure 8d. The admittance from the GRAIL data could be used to infer the crustal density when the correlation is high. (The unity in the admittance computation corresponds to 2550 kg/m$^3$). For the frequencies between 15 and 45 mHz ($L = 100$–$300$), the correlation with the topography potential is nearly unity, implying the gravity anomaly is most likely from topography anomaly, and the admittance is consistent around unity or with a slightly decreasing trend, implying the introduced density 2550 kg/m$^3$ reproduce the GRAIL observation of LOS gravity difference in this band. Due to the increasing data noise, the admittance estimates beyond 60 mHz or degree 400 (not shown) are too noisy.

[35] The same computation was applied to the data acquired during 23–28 May 2012, covering the same area as in Figure 8, but the orbit was higher (~90 km) over the nearside and lower (~20 km) over the farside, as shown in Figure 9a. Therefore, the power and cross-power spectrum computations are biased by the low-altitude data and thus effectively represent the central farside (bluish region in Figure 9a). The power

spectrum of the GRAIL L1B observation follows the one computed from the LOLA topography potential model out to 0.1 Hz (degree 660). The Bouguer anomaly spectrum seems to degrade starting from 83 mHz (degree 550), higher than the previous case. The (local) correlation of L1B LOS gravity difference observables yields almost unity to 83 mHz ($L = 550$) and becomes 0.9 around 94 mHz ($L = 620$) as shown in Figure 9c, while the (global) topography correlation of the L2 gravity model in *Zuber et al.* [2013a] deviates from unity around degree 320 and becomes 0.9 around degree 370. This result indicates that the LOS gravity difference data contain information up to degree 660 over various regions covered by low-altitude orbits, substantially higher than the global estimates given in *Zuber et al.* [2013a]. In fact, *Konopliv et al.* [2013] shows the space-dependent resolution of their global gravity field solution that yields sensitivity to degree 580 over certain regions including the one I examined in Figure 9.

[36] The admittance spectrum is consistent with the previous case up to 45 mHz ($L = 300$) with less noise, but the low-orbit data yield the admittance close to the unity (with a slightly decreasing trend) up to 60 mHz (degree 400). A substantial decreasing trend from 60 to 90 mHz ($L = 400$–$600$) was observed while the correlation at this band is still close to unity. The radial stratification of the crustal density may cause such degree-dependent variation in the admittance while the correlation is less affected. Higher-degree gravity signal is more influenced by shallower mass anomalies; a
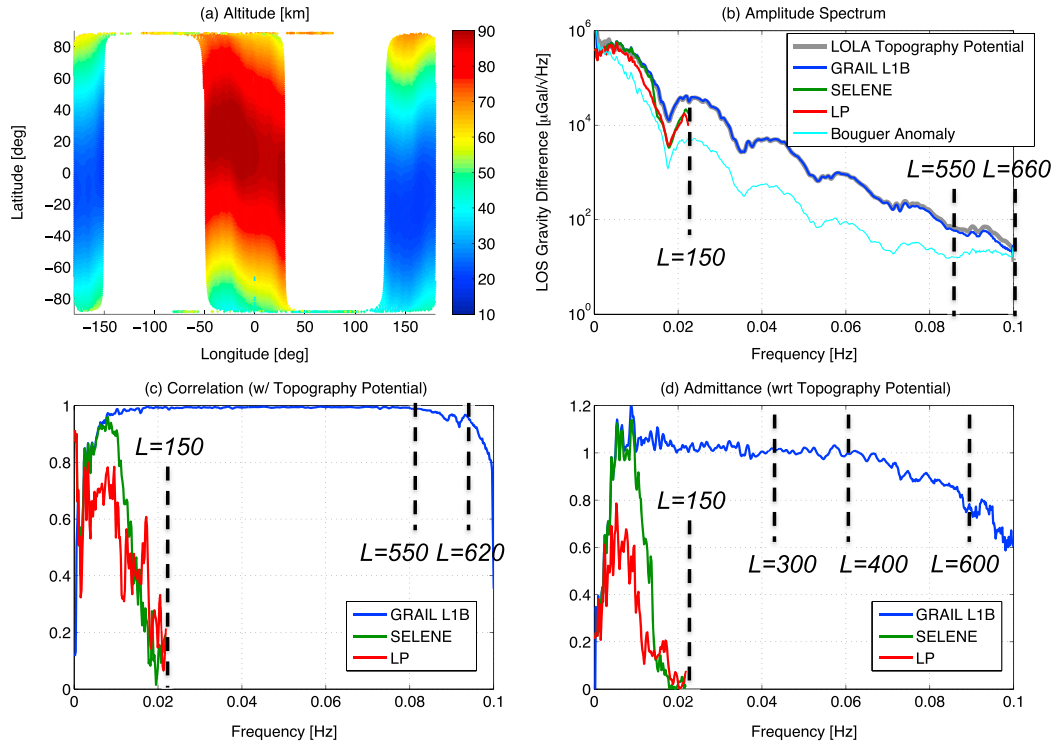
**Figure 9.** Same as Figure 8 but for the period from 23 to 28 May 2012. Note that the ground coverage is the same as Figure 8, but the altitudes are higher at the nearside and lower at the farside. The spectral estimates are strongly biased by the farside data at low altitude.

simplified model relating the depth and degree is suggested in *Bowin* [1983]. In the next section, I discuss the spatially and radially variable density structure as estimated from the GRAIL data at different degree bands.

[37] Two LOS gravity data sets used in Figure 8 (April data with altitudes of $55 \pm 10$ km) and in Figure 9 (May data with altitudes of 20–90 km) were also compared after applying the band-pass filters to highlight the signals at the frequency band of 23–45 mHz ($L = 150$–300) and of 45–75 mHz ($L = 300$–500), separately. The first band is similar to the one used in *Wieczorek et al*. [2013a] to infer the crustal

density. The second band was not examined because it was noisy in the global gravity field solutions from the primary mission [*Zuber et al*., 2013a]. Figure 10a presents the GRAIL data at 23–45 mHz, in April and May separately, highlighting the gravity signals at $L = 150$–300. Figure 10b shows the same data sets but at 45–75 mHz ($L = 300$–500). The geographical areas for these data are identical as shown in Figures 8a and 9a. The gravitational signal attenuates with altitude while the data noise does not. The higher-frequency signals (Figure 10b) attenuate greater than the lower frequency signals (Figure 10a) with increasing altitude. In the
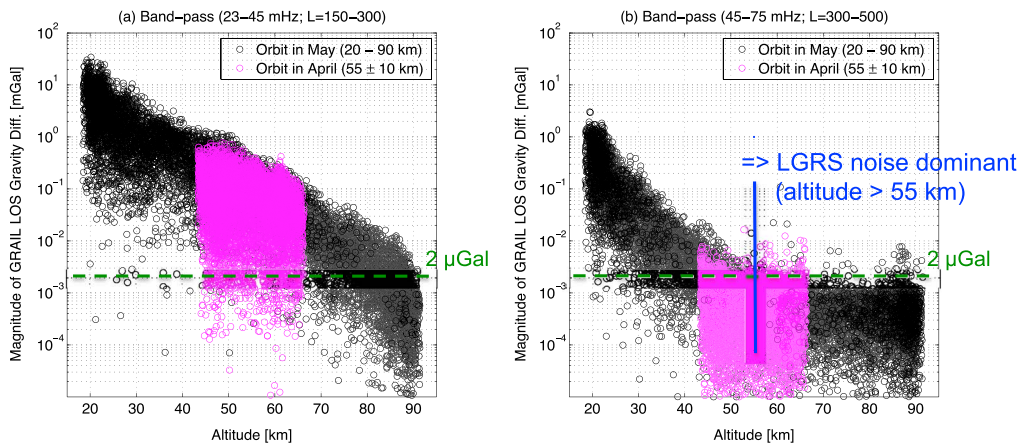


**Figure 10.** The GRAIL LOS gravity difference data used in Figures 8 and 9 (the one with altitudes $55 \pm 10$ km and the other with altitudes 20–90 km) are shown over altitudes and at two different frequency bands. The band-pass filtering was applied to the time series data to highlight the signals corresponding to $L = 150$–300 (or 23–45 mHz) and 300–500 (or 45–75 mHz), separately.
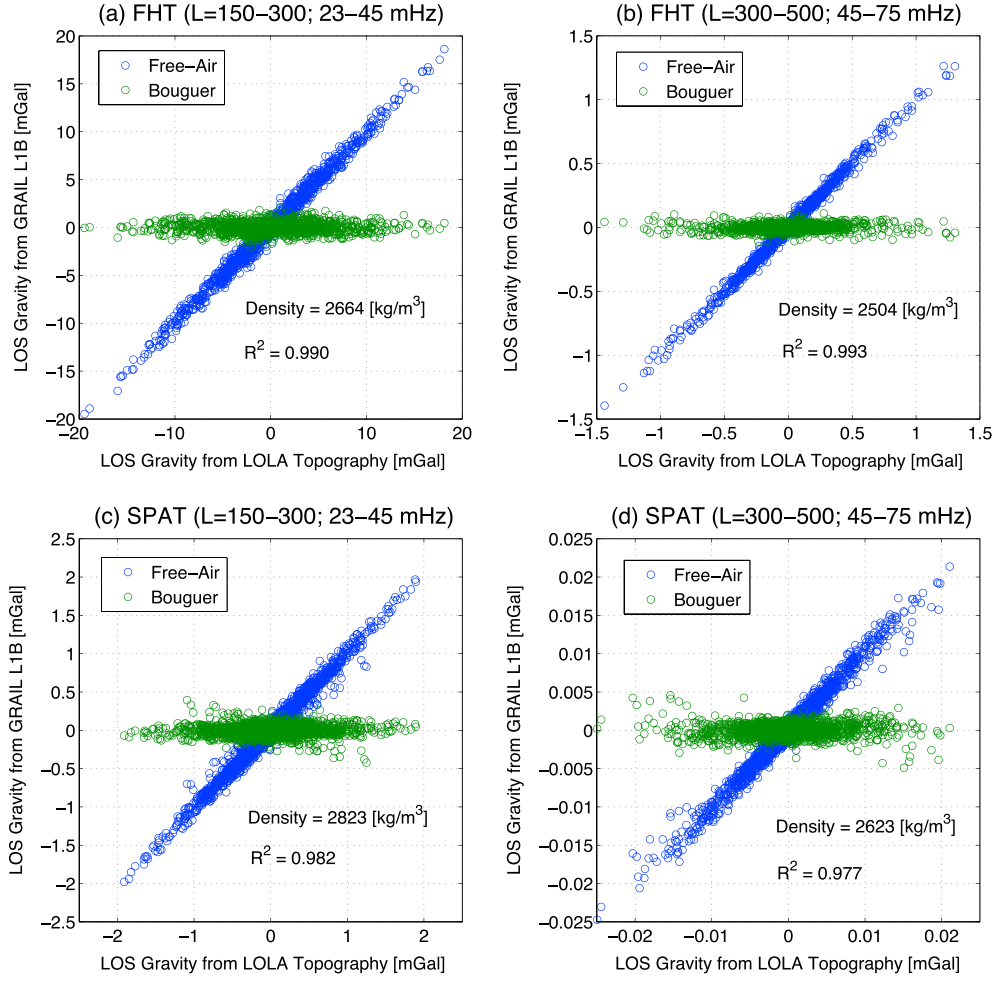
**Figure 11.** Comparison of GRAIL L1B data and LOLA topography potential model in terms of LOS gravity difference. Only the low-altitude data ($< 55$ km) in May 2012 were used over two different regions, Feldspathic High Land Terrane (FHT) and South Pole-Aitken Terrane (SPAT). The density at each region was estimated from the GRAIL data at two different degree bands. $R^2$ values are $> 0.98$ for all cases.

lower frequency band, the signals are dominant at all altitudes to 90 km. However, in the higher-frequency band, the LGRS instrument noise becomes dominant when the altitude is higher than 55 km and approaches to 1–2 µGal.

## 6. Estimation of Crustal Density From LOS Gravity Difference and Topography

[38] In this section, I discuss how the LOS gravity difference data can be used to examine the crustal density and its lateral and vertical variability. The density $\gamma$ is a scaling factor to the topographic potential via equation (10) and hence to the Bouguer correction via equation (11). Therefore, one can derive the density by comparing the LOS gravity difference observations and the synthetics with topography. The linear model can be written as

$$g_{\mathrm{LOS}} = \gamma p_{\mathrm{LOS}} + \varepsilon. \qquad (13)$$

[39] Note that $p_{\mathrm{LOS}}$ is completely determined by the topography and orbit data and $g_{\mathrm{LOS}}$ is the GRAIL observation contaminated by the LGRS measurement noise $\varepsilon$. This model assumes that the gravity signals are solely from the topography variation. Other complex geophysical processes such as lithospheric flexure, dynamic topography, and mantle heterogeneity are limited to relatively low degree (degree 150 or less for the Moon) [*Wieczorek et al.*, 2013a], and the uncompensated topography should manifest in the gravity anomaly at higher degrees. This becomes apparent in nearly unity correlation of the GRAIL L2 global gravity solution with topography at the degree band ($L = 150$–$300$) [*Zuber et al.*, 2012] and in the local results extending to degree 550 directly from L1B data (Figure 9c).

[40] Therefore, the model given in equation (13) is valid only for the band-limited gravity and topography data when they are correlated. I obtain the least squares solution of the density parameter that minimizes the measurement noise $\varepsilon$ (or equivalently, the Bouguer anomaly $g_{\mathrm{LOS}} - \gamma p_{\mathrm{LOS}}$) from the bandpass filtered time series of the GRAIL data and topography synthetics. In this case, the solution also minimizes the Bouguer coherence (i.e., squared correlation between the Bouguer anomaly $g_{\mathrm{LOS}} - \gamma p_{\mathrm{LOS}}$ and the topography effect $p_{\mathrm{LOS}}$).

[41] The lunar crust exhibits strong lateral heterogeneity in density (both porosity and composition) with complex mixture of impact bombardment and volcanism. I examine the lateral
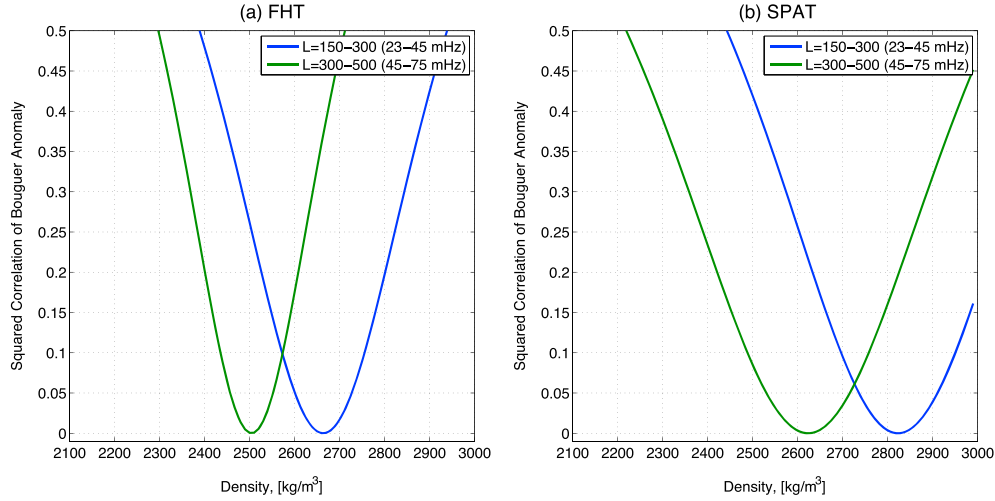
**Figure 12.** The coherence (squared correlation) between the Bouguer anomaly $g_{LOS} - g_{LOS}^B(\gamma)$ and Bouguer correction $g_{LOS}^B(\gamma)$ computed with variation in density $\gamma$. The bulk density estimate is found when the coherence shows its minimum. It represents the effective density over the region over FHT and SPAT (the same area used in Figure 11). I show the results at two different spectral bands ($L = 150$–$300$ and $L = 300$–$500$).

density variation using the regional set of the data and its frequency dependence (possibly due to radial density variation) by applying two different band-pass filters. I chose two distinct regions: Feldspathic Highland Terrane (FHT) and South Pole-Aitken Terrane (SPAT) from *Jolliff et al.* [2000], which are delineated by spherical caps with a radius of 10° centered at 30°N, 150°W and at 60°S, 160°W, respectively. I applied the band-pass filter to the daily time series at the frequency bands of 23–45 mHz (equivalently, $L = 150$–$300$ in spherical harmonic degree band) and 45–75 mHz ($L = 300$–$500$) for identification of radial density stratification reflected in the frequency dependence of the regional density estimates. I used the entire primary mission data from March to May in 2012 but limited at the altitudes below 55 km and confined within each of the spherical cap regions (FHT and SPAT).

[42] The (free air) LOS gravity difference data from GRAIL were highly correlated with the ones predicted by LOLA topography in both degree bands at two different regions, FHT and SPAT, as shown in Figure 11. In each region, the density was estimated by the least squares inversion of the entire primary mission data. Over FHT, the estimated density is 2664 and 2504 kg/m$^3$ for $L = 150$–$300$ and 300–500, respectively. Over SPAT, it is 2823 and 2623 kg/m$^3$ for $L = 150$–$300$ and 300–500, respectively. To determine the error bound of the density estimates, I obtained three additional density solutions for each case from the data in March, April, and May, separately. These density solutions are consistent within 30–40 kg/m$^3$. In general, the density of the anorthositic FHT is estimated to be 5% lower than that of the mafic SPAT, consistently for both degree bands. In both regions, the density solutions at the higher-degree band are 6–7% smaller than those at the lower degree band. I also computed the Bouguer coherence by varying densities from 2000 to 3000 kg/m$^3$ for FHT and SPAT and for each degree band (Figure 12). The minimum Bouguer coherence is found with the density solution obtained from the above least squares solutions.

[43] I extended the density analysis over the entire globe. First, the mean correlation of the GRAIL LOS gravity difference data with the LOLA topography potential along the trajectory (in a spatial domain) was computed within a spherical cap region with the radius of 8°. The cap center was moved by 2° in latitude and by the equal distance in longitude over the globe. Figures 13a and 13b show the spatial variability of the correlation at two different frequency bands. For the data band-pass filtered within 23–45 mHz, the high correlation ($> 0.95$) was found over most of the globe. The low correlation ($< 0.95$) was limited over the Procellarum KREEP Terrane (PKT) where the fractional value of FeO weight is larger than 12% (Figure 13c) and where the Th content is also relatively high ($> 3.5$ ppm) [*Jolliff et al.*, 2000]. The correlation is relatively low over SPAT in comparison to the other farside regions. Flood basalts in the PKT infilled ancient surface topography and have produced considerable heterogeneity in surface terranes, creating a complex response to gravity and reducing the gravity-topography correlation. For the data at the higher-frequency band of 45–75 mHz, the low correlation extends over the polar regions and the area between 70°E and 120°E where the low-altitude data are limited during the primary mission and hence the GRAIL data show less sensitivity to the high-frequency gravity (See also Figure 6 of *Konopliv et al.* [2013] and Figure 2 *Lemoine et al.* [2013]). The mean correlation separately from monthly data of March, April, and May in 2012 is shown in the supporting information Figures S1 and S2.

[44] In equation (13), $g_{LOS}$ is the filtered time series of GRAIL data while $p_{LOS}$ is from the topography synthetics. The unknown density $\gamma$ is merely a scale factor of the linear model between the GRAIL data and LOLA synthetics. This scale factor is determined from the least square inversion of equation (13), using the data at each spherical cap region. The GRAIL data at two different frequency bands were inverted, separately, to estimate the density. The density solution also minimizes the Bouguer coherence at the region. The
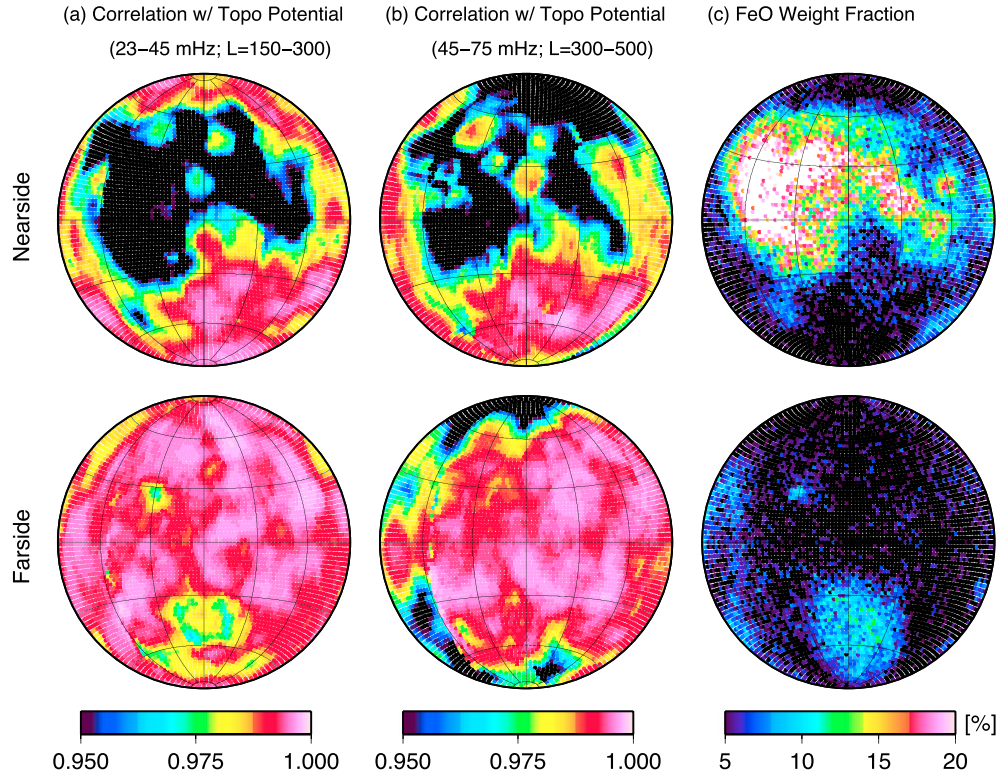
**Figure 13.** (a, b) The correlation between the LOLA topographic potential and the GRAIL LOS gravity difference. (c) The FeO weight fraction from *Jolliff et al.* [2000] (shown are the PDS Geosciences Node data binned on 2° equal area pixel).
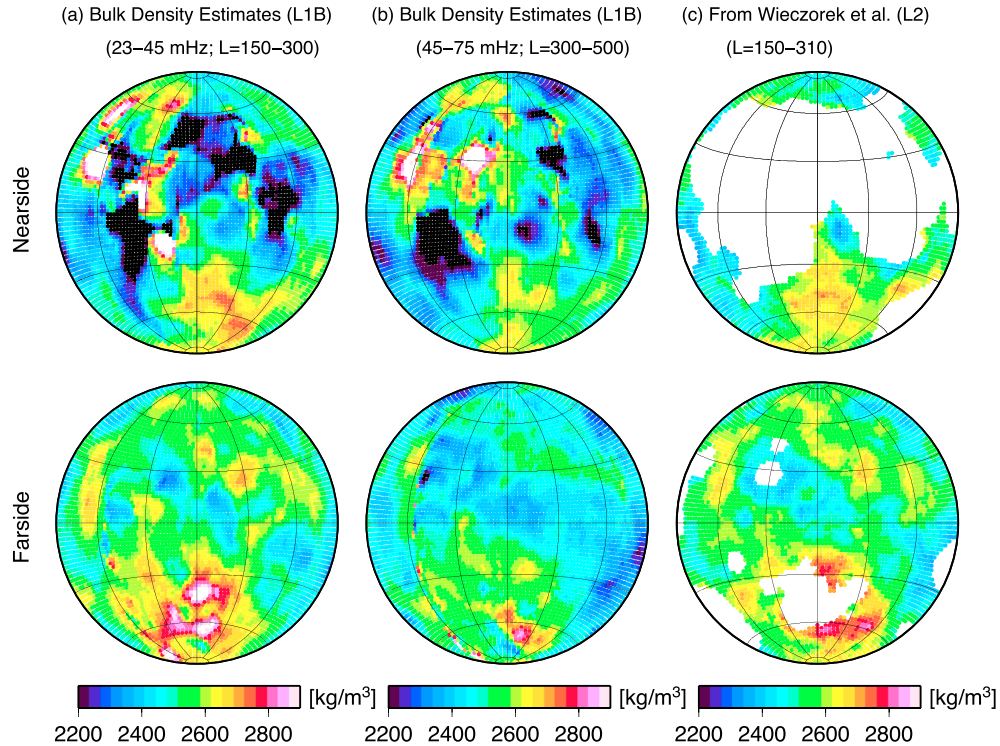


**Figure 14.** (a, b) The density estimates from the data at the low-frequency band (23–45 mHz or $L = 150–300$) and the high-frequency band (45–75 mHz or $L = 300–500$), respectively. Note that these density solutions must be interpreted only where the correlation in Figure 13 is close to unity. (c) The independent density solutions from *Wieczorek et al.* [2013a].
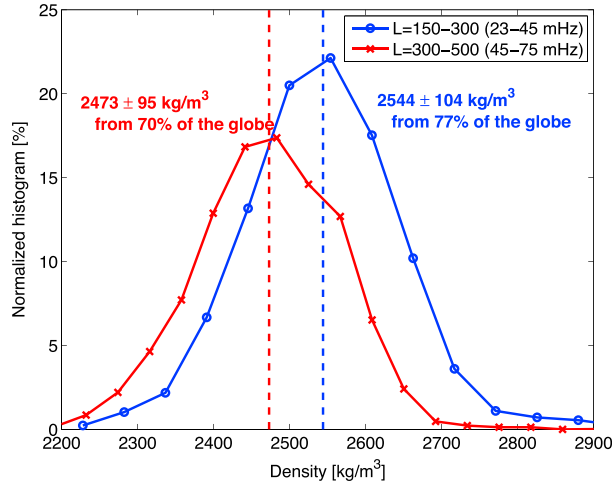
**Figure 15.** The histogram of the density estimates over the globe, shown in Figures 14a and 14b, separately from two different degree bands. The global mean density from each band is shown in the vertical dashed bar. The density solutions with the correlation 0.95 or larger were used. They cover 70–80% of the globe depending on the frequency band.

density estimates over the globe are shown in Figures 14a and 14b, for the lower and higher-frequency band, respectively. Each of them must be interpreted, in conjunction with Figure 13, only when the corresponding correlation is close to unity. Excluding the density solutions with the lower correlation ($> 0.95$), the least squares formal error is in general smaller than 20 kg/m$^3$. Therefore, the spatial variation of density ranging from 2200 to 2900 kg/m$^3$ is statistically significant. For the lower frequency band (23–45 mHz or $L = 150$–300), the highest density is found from SPAT while the lowest density is found from the surrounding areas of the Mare Orientale and Mare Moscoviense. Over the Southern Hemisphere of the nearside, the relatively high density (~2700 kg/m$^3$) is found. For the higher-frequency band (45–75 mHz or $L = 300$–500), the total area of the high correlation ($> 0.95$) is reduced as shown in Figure 13. The overall spatial pattern of the density distribution is similar to the one from the lower frequency band; however, the absolute magnitude of density at each region is reduced roughly by 100 kg/m$^3$, as shown in Figure 14b. The lowest density (2300–2400 kg/m$^3$) prevails over the farside highlands surrounding the South Pole-Aitken basin.

[45] In order to test the consistency of the density solutions, I estimated the global density distribution using only the monthly L1B data in March, April, and May, separately. The spatial patterns of three solutions are consistent as shown in the supporting information Figures S3 and S4. The density solutions with higher correlation ($> 0.95$) agree each other within 35 and 27 kg/m$^3$ for the frequency bands 23–45 and 45–75 mHz, respectively. These are the upper bound errors of the density estimates from the entire primary mission data (Figure 14).

[46] The density solution inverted from the L1B data at the low-frequency band (Figure 14a) agrees with the result obtained by *Wieczorek et al.* [2013a] from the analysis of L2 global gravity solution (shown in Figure 14c and supporting information Figure S5). When the common grid

points are taken, two independent solutions agree with a correlation coefficient of 0.74 and a difference of 63 kg/m$^3$ (standard deviation) presenting insignificant systematic and mean difference of 3 kg/m$^3$. The difference is certainly larger than the error bound of 35 kg/m$^3$ I obtained from the monthly subsamplings. This is partly due to the fact that (i) *Wieczorek et al.* [2013a] did not use the L2 gravity data within the maria for the density estimation while I used the entire L1B data; (ii) The band-pass filter I apply in the time domain is only the approximation to the one in the spherical harmonic domain; (iii) Spatial averaging of the L1B data within the spherical cap is not the same as that of the L2 gravity data points, due to variations in altitude (20–90 km) and in distance between two satellites (80–220 km).

[47] A histogram of the density estimates over the globe is computed from both bands and compared in Figure 15. Again, only the solutions yielding high correlation ($> 0.95$) were used. Total 70–80% of the globe was included depending on the frequency band. For the degree band 150–300, the mean density of 2544 kg/m$^3$ with the lateral variation of $\pm 312$ kg/m$^3$ ($3 - \sigma$) is found from the analysis of the GRAIL LOS gravity difference data. The mean density and the range of its spatial variability agree well with *Wieczorek et al.* [2013a]. For the higher-degree band of 300–500, the mean density is 2473 kg/m$^3$ and the lateral variation is within $\pm 285$ kg/m$^3$. The bulk density estimates from the higher-degree band data are globally 3% smaller than the ones from the lower degree band data. This result indeed confirms *Wieczorek et al.* [2013b] that found the degree dependence of density estimates (2550 kg/m$^3$ for degrees near 200 and 2450 kg/m$^3$ for degrees near 400 in their Figure 2) using the analysis of the extended mission gravity field solutions.

## 7. Summary and Discussion

[48] I present a rigorous model to process the readily available L1B data products to derive measurements of intersatellite LOS gravity difference at altitudes. In addition to KBR ranging data, the orbit data are equally important to retrieve the gravitational measurement from the geometric (i.e., range acceleration) measurement and to align the LOS gravity difference data especially in altitude. The errors caused by the imperfect orbit data presently available in PDS and the LGRS instrumental noise are some μGal in terms of LOS gravity difference at 0.1 Hz, or equivalently, spherical harmonic degree 660. The correction by the orbit data (through the term $\dot{\mathbf{x}}_{12} \cdot \dot{\mathbf{e}}_{12}$) needs to be applied to the range-acceleration data set to obtain the gravity signal. Otherwise, the systematic errors with the magnitude of several percentages of the gravity signal would exist. However, such correction becomes less critical for degrees higher than 400.

[49] I analyzed the L1B data from the primary mission, independently from the GRAIL science team, and processed for the LOS gravity difference to quantify the correlation with topography and to estimate the bulk crustal density. I verified that the low-orbit data, amounting 30% of the total primary mission data, could be sensitive to degree 660 but might not be optimally utilized in construction of the L2 global gravity models especially due to the applied power constraint. The L1B data correlation with topography potential was nearly unity to degree 550 and became 0.9 around

degree 620 over certain areas covered by low-altitude orbits during the primary mission. The Bouguer anomaly was computed, in terms of LOS gravity difference, along the orbit by upward continuation of the topographic potential model. It was found that the bulk density of 2500–2600 kg/m$^3$ minimizes the coherence between the GRAIL Bouguer anomaly and the LOLA topography potential. The density estimates show substantial lateral variation by about 10%, being higher at the mafic South Pole-Aitken Basin and lower at the anorthositic highland.

[50] In addition, the systematic decrease in the bulk density estimate is observed at higher degrees. The higher-degree band is more sensitive to the density anomaly at the shallower layer [*Bowin*, 1983]. This lower density estimates from the higher-degree band (lowered by 3% or 71 kg/m$^3$) imply the inadequacy of topography potential model with uniform density across the entire lithosphere and suggest radial stratification of the bulk density (or porosity) such as a pulverized megaregolith layer and its compaction with depth. *Wieczorek et al.* [2013a, 2013b] and *Besserer et al.* [2013], originally from *Nimmo et al.* [2003], introduced a theoretical depth-dependent porosity (and thus bulk density) model. The higher-degree gravity observation from this study and more definitely from the extended mission data should be invaluable to constrain various parameters in the proposed pore closure model.

[51] The LOS analysis presented in this study is based on the one-dimensional Fourier transforms of the GRAIL L1B data and LOLA topography synthetics without using the geometrical constraint of neighboring tracks. The analysis can be improved by computing the two-dimensional grid of the LOS data to calculate the spectra [*McKenzie and Nimmo*, 1997] and by estimating the regional gravity solutions with the localized harmonic basis functions [*Han*, 2008]. The LOS technique may be even more beneficial to the analysis of GRAIL extended mission data at lower altitudes (23 ± 12 km), which are potentially sensitive to very high degrees like 900 or higher. The orbit data error is a primary concern for precise determination of the LOS gravity difference data at such low altitudes to the LGRS measurement noise level. Due to spatially localized characteristic, the LOS gravity difference data are suited particularly to the regional analysis at the highest-possible resolution. The LOS gravity difference data product will make the raw L1B data more accessible to the science community and allow geophysical modeling and analysis directly from L1B and thus will expand the science return from the GRAIL mission.

## Appendix A: LOS Gravity Modeling Error From Equation (6)

[52] The upper bound of three error terms in equation (6) is quantified in terms of the relative position and velocity vector errors.

[53] The first term $(\tilde{\mathbf{g}}_{12}) \cdot \delta\mathbf{e}_{12}$ is caused by error in relative position vector $\delta\mathbf{x}_{12}$. It should be bounded by $|\tilde{\mathbf{g}}_{12}||\delta\mathbf{e}_{12}|$. Along the actual GRAIL orbits, $|\tilde{\mathbf{g}}_{12}|$ without the central or degree-zero term (a point mass gravity term; $GM/a^2$) ranges from 100 to 300 mGal depending on altitude. The central term causes the substantially larger anomaly with a magnitude of

~0.1 m/s$^2$ at the one cycle-per-revolution (1 cpr) frequency. For $|\delta\mathbf{e}_{12}|$, I obtain $\mathbf{e}_{12} = \frac{\mathbf{x}_{12}}{\rho} \approx \tilde{\mathbf{e}}_{12} + \frac{\delta\mathbf{x}_{12}}{\tilde{\rho}} - \frac{\tilde{\mathbf{x}}_{12}\delta\rho}{\tilde{\rho}^2}$ and thus $|\delta\mathbf{e}_{12}| < \frac{|\delta\mathbf{x}_{12}|}{\tilde{\rho}} + \frac{|\delta\rho|}{\tilde{\rho}} \sim \frac{|\delta\mathbf{x}_{12}|}{100 \text{ km}}$, when I use $|\delta\mathbf{x}_{12}| > |\delta\rho|$ and $\tilde{\rho} = 100$ km. Therefore, $(\tilde{\mathbf{g}}_{12}) \cdot \delta\mathbf{e}_{12} < 10^{-6}|\delta\mathbf{x}_{12}|$ m/s$^2$, when the relative position error $|\delta\mathbf{x}_{12}|$ is given in meter.

[54] The second term, $(\tilde{\mathbf{e}}_{12}) \cdot \delta\dot{\mathbf{x}}_{12}$, is caused by error in relative velocity vector $\delta\dot{\mathbf{x}}_{12}$. From the actual GRAIL satellite orbits (available as a part of L1B data), I obtain $\tilde{\mathbf{e}}_{12} \sim \pm 10^{-3}$ s$^{-1}$ mostly at the 1 cpr frequency (~0.15 mHz) and $\tilde{\mathbf{e}}_{12} \sim \pm 10^{-5}$ s$^{-1}$ at the higher-frequency band (greater than 0.3 mHz). Therefore, $(\tilde{\mathbf{e}}_{12}) \cdot \delta\dot{\mathbf{x}}_{12} < 10^{-3}|\delta\dot{\mathbf{x}}_{12}|$ m/s$^2$ when the relative velocity error $|\delta\dot{\mathbf{x}}_{12}|$ is given in m/s.

[55] The third term, $(\tilde{\dot{\mathbf{x}}}_{12}) \cdot \delta\dot{\mathbf{e}}_{12}$, is caused by mixture of relative position and velocity errors, $\delta\mathbf{x}_{12}$ and $\delta\dot{\mathbf{x}}_{12}$, since $\delta\dot{\mathbf{e}}_{12} = \delta(\dot{\mathbf{x}}_{12}/\rho) - \delta(\dot{\rho}\mathbf{e}_{12}/\rho)$. For GRAIL, the relative velocity variation is bound by 100 m/s ($\tilde{\dot{\mathbf{x}}}_{12} \sim \pm 100$ m/s) and characterized with the 1 cpr frequency. However, it is reduced to $\tilde{\dot{\mathbf{x}}}_{12} \sim \pm 1$ m/s at the higher frequency beyond 1 cpr. Therefore, $(\tilde{\dot{\mathbf{x}}}_{12}) \cdot \delta\dot{\mathbf{e}}_{12} < 10^2|\delta\dot{\mathbf{e}}_{12}|$ m/s$^2$ when $|\delta\dot{\mathbf{e}}_{12}|$ is given in s$^{-1}$. $\delta\dot{\mathbf{e}}_{12}$ is written as $\delta\dot{\mathbf{e}}_{12} = \left( \frac{\delta\dot{\mathbf{x}}_{12}}{\tilde{\rho}} - \frac{\tilde{\dot{\mathbf{x}}}_{12}\delta\rho}{\tilde{\rho}^2} \right) - \left( \frac{\tilde{\dot{\rho}}\delta\mathbf{e}_{12}}{\tilde{\rho}} + \frac{\tilde{\mathbf{e}}_{12}\delta\dot{\rho}}{\tilde{\rho}} - \frac{\tilde{\dot{\rho}}\tilde{\mathbf{e}}_{12}\delta\rho}{\tilde{\rho}^2} \right)$, and thus

$$|\delta\dot{\mathbf{e}}_{12}| < \left| \frac{\delta\dot{\mathbf{x}}_{12}}{\tilde{\rho}} \right| + \left| \frac{\tilde{\dot{\mathbf{x}}}_{12}\delta\rho}{\tilde{\rho}^2} \right| + \left| \frac{\tilde{\dot{\rho}}\delta\mathbf{e}_{12}}{\tilde{\rho}} \right| + \left| \frac{\tilde{\mathbf{e}}_{12}\delta\dot{\rho}}{\tilde{\rho}} \right| + \left| \frac{\tilde{\dot{\rho}}\tilde{\mathbf{e}}_{12}\delta\rho}{\tilde{\rho}^2} \right|$$

$$< \frac{1}{\tilde{\rho}}|\delta\dot{\mathbf{x}}_{12}| + \frac{|\tilde{\dot{\mathbf{x}}}_{12}|}{\tilde{\rho}^2}|\delta\rho| + \frac{\tilde{\dot{\rho}}}{\tilde{\rho}}|\delta\mathbf{e}_{12}| + \frac{1}{\tilde{\rho}}|\delta\dot{\rho}| + \frac{\tilde{\dot{\rho}}}{\tilde{\rho}^2}|\delta\rho|,$$

$$< \frac{2}{\tilde{\rho}}|\delta\dot{\mathbf{x}}_{12}| + \frac{|\tilde{\dot{\mathbf{x}}}_{12}|}{\tilde{\rho}^2}|\delta\mathbf{x}_{12}| < 1 \times 10^{-8}|\delta\mathbf{x}_{12}| + 2 \times 10^{-5}|\delta\dot{\mathbf{x}}_{12}|$$

where I used $|\delta\dot{\mathbf{x}}_{12}| > |\delta\dot{\rho}|$, $|\delta\mathbf{x}_{12}| > |\delta\rho|$, $\tilde{\rho} \approx 100$ km, and $\tilde{\dot{\rho}} \approx 1$ m/s . Therefore, $(\tilde{\dot{\mathbf{x}}}_{12}) \cdot \delta\dot{\mathbf{e}}_{12} < 1 \times 10^{-6}|\delta\mathbf{x}_{12}| + 2 \times 10^{-3}|\delta\dot{\mathbf{x}}_{12}|$ m/s$^2$.

## References

Asmar, S. W., et al. (2013), The Scientific Measurement System of the Gravity Recovery and Interior Laboratory (GRAIL) Mission, *Space Sci. Rev.*, Published Online 21 Feb 2013, *174*, doi:10.1007/s11214-013-9962-0

Barriot, J. P., N. Vales, G. Balmino, and P. Rosenblatt (1998), A 180th degree and order model of the Venus gravity field from Magellan line of sight residual Doppler data, *Geophys. Res. Lett.*, *25*, 3743–3746.

Besserer, J., F. Nimmo, M. A. Wieczorek, W. S. Kiefer, J. Andrews-Hanna, and M. T. Zuber (2013), Theoretical and observational constraints on lunar

mega-regolith thickness, Abstract #2463, A paper presented at 44th Lunar and Planetary Science Conference, Huston, TX.

Beuthe, M., P. Rosenblatt, V. Dehant, J.-P. Barriot, M. Pätzold, B. Häusler, Ö. Karatekin, S. Le Maistre, and T. Van Hoolst (2006), Assessment of the Martian gravity field at short wavelength with Mars Express, *Geophys. Res. Lett.*, *33*, L03203, doi:10.1029/2005GL024317.

Beuthe, M., S. Le Maistre, P. Rosenblatt, M. Pätzold, and V. Dehant (2012), Density and lithospheric thickness of the Tharsis Province from MEX MaRS and MRO gravity data, *J. Geophys. Res.*, *117*, E04002, doi:10.1029/2011JE003976.a

Bowin, C. (1983), Depth of principal mass anomalies contributing to the Earth's geoid undulations and gravity anomalies, *Mar. Geod.*, *7*, 61–100, doi:10.1080/15210608309379476.

Crossby, A., and D. McKenzie (2005), Measurements of the elastic thickness under ancient lunar terrain, *Icarus*, *173*, 100–107.

Goossens, S., P. N. A. M. Visser, and B. A. C. Ambrosius (2005), A method to determine regional lunar gravity fields from earth-based satellite tracking data, *Planet. Space Sci.*, *53*, 1331–1340.

Goossens, S., et al. (2011), Improved high-resolution lunar gravity field model from SELENE and historical tracking data, AGU Fall Meeting, Abstract P44B-05, 2011.

Han, S.-C. (2008), Improved regional gravity fields on the Moon from Lunar Prospector tracking data by means of localized spherical harmonic functions, *J. Geophys. Res.*, *113*, E11012, doi:10.1029/2008JE003166.

Han, S.-C., C. K. Shum, and C. Jekeli (2006), Precise estimation of in situ geopotential differences from GRACE low-low satellite-to-satellite tracking and accelerometer data, *J. Geophys. Res.*, *111*, B04411, doi:10.1029/2005JB003719.

Han, S.-C., E. Mazarico, and F. G. Lemoine (2009), Improved nearside gravity field of the Moon by localizing the power law constraint, *Geophys. Res. Lett.*, *36*, L11203, doi:10.1029/2009GL038556.

Han, S.-C., E. Mazarico, D. Rowlands, F. Lemoine, and S. Goossens (2011), New analysis of Lunar Prospector radio tracking data brings the nearside gravity field of the Moon with an unprecedented resolution, *Icarus*, *215*, 455–459, doi:10.1016/j.icarus.2011.07.020.

Jekeli, C. (1999), The determination of gravitational potential differences from satellite-to-satellite tracking, *Celest. Mech. Dyn. Astr.*, *75*, 85–101.

Jolliff, B. L., J. J. Gillis, L. A. Haskin, R. L. Korotev, and M. A. Wieczorek (2000), Major lunar crustal terranes: Surface expressions and crust-mantle origins, *J. Geophys. Res.*, *105*, 4197–4216.

Kaula, W. M. (1996), Regional gravity fields on Venus from tracking of Magellan cycles 5 and 6, *J. Geophys. Res.*, *101*, 4683–4690.

Killett, B., J. Wahr, S. Desai, D. Yuan, and M. Watkins (2011), Arctic Ocean tides from GRACE satellite accelerations, *J. Geophys. Res.*, *116*, C11005, doi:10.1029/2011JC007111.

Kim, J. (2000), Simulation study of a low-low satellite-to-satellite tracking mission. PhD dissertation, Univ. of Texas at Austin, May 2000.

Konopliv, A. S., S. W. Asmar, E. Carranza, W. L. Sjogren, and D. N. Yuan (2001), Recent gravity models as a result of the lunar prospector mission, *Icarus*, *150*, 1–18.

Konopliv, A. S., et al. (2013), The JPL lunar gravity field to spherical harmonic degree 660 from the GRAIL Primary Mission, *J. Geophys. Res. Planets*, *118*, 1415–1434, doi:10.1002/jgre.20097.

Kruizinga, G., et al. (2013), The role of GRAIL orbit determination in pre-processing of gravity science measurements, AAS 13–270, A paper presented at the 23rd AAS/AIAA Space Flight Mechanics Meeting, Kauai, Hawaii, February 10 – 14, 2013.

Lemoine, F. G., et al. (2013), High-degree gravity models from GRAIL Primary mission data, *J. Geophys. Res. Planets*, *118*, 1676–1698, doi:10.1002/jgre.20118 in press.

Mayer-Gürr, T., A. Eicker, and K. H. Ilk (2006), Gravity field recovery from GRACE-SST data of short arcs, in *Observation of the Earth System from Space*, edited by J. Flury et al., pp. 131–148 , Springer, Berlin.

McKenzie, D., and F. Nimmo (1997), Elastic thickness estimates for Venus from line of sight accelerations, *Icarus*, *130*, 198–216.

McKenzie, D., D. N. Barnett, and D.-N. Yuan (2002), The relationship between Martian gravity and topography, *Earth Planet. Sci. Lett.*, *195*, 1–16.

Moyer, T. D. (2005), Formulation for observed and computed values of deep space. Network Data Types for Navigation, Hoboken, NJ.

Nimmo, F., R. T. Pappalardo, and B. Giese (2003), On the origins of band topography, Europa, *Icarus*, *166*, 21–32, doi:10.1016/j.icarus.2003.08.002.

Pavlis, D. E., S. G. Poulouse, and J. J. McCarthy (2009), GEODYN Operations Manuals SGT, Inc., Greenbelt, MD.

Ramillien, G., R. Biancale, S. Gratton, X. Vasseur, and S. Bourgogne (2011), GRACE-derived surface water mass anomalies by energy integral approach: Application to continental hydrology, *J. Geodesy*, *85*, 313–328, doi:10.1007/s00190-010-0438-7.

Rowlands, D., S. Luthcke, S. Klosko, F. Lemoine, D. Chinn, J. McCarthy, C. Cox, and O. Anderson (2005), Resolving mass flux at high spatial and temporal resolution using GRACE intersatellite measurements, *Geophys. Res. Lett.*, *32*, L04310, doi:10.1029/2004GL021908.

Smith, D. E., et al. (2010), Initial observations from the Lunar Orbiter Laser Altimeter (LOLA), *Geophys. Res. Lett. 37*, L18204, doi:10.1029/2010GL043751.

Sugano T., and K. Heki (2004), Isostasy of the Moon from high-resolution gravity and topography data: Implication for its thermal history, *Geophys. Res. Lett.*, *31*, L24703, doi:10.1029/2004GL022059.

Tapley, B. D., S. Bettadpur, M. Watkins, and C. Reigber (2004), The gravity recovery and climate experiment: Mission overview and early results, *Geophys. Res. Lett.*, *31*, L09607, doi:10.1029/2004GL019920.

Welch, P. D. (1967), The use of fast Fourier transform for the estimation of power spectra: A method based on time averaging over short, modified periodograms, *IEEE Trans. Audio Electroacoust.*, *AU-15*, 70–73.

Wieczorek, M. A., and R. J. Phillips (1998), Potential anomalies on a sphere: Applications to the thickness of the lunar crust, *J. Geophys. Res.*, *103*, 1715–1724, doi:10.1029/97JE03136.

Wieczorek, M. A., et al. (2013a), The crust of the Moon as seen by GRAIL, *Science*, *339*, 671–675, doi:10.1126/science.1231530.

Wieczorek, M. A., et al. (2013b), High-resolution estimates of lunar crustal density and porosity from the GRAIL extended mission, Abstract #1914, A paper presented at 44th Lunar and Planetary Science Conference, Huston, TX.

Williams, J.-P., F. Nimmo, W. B. Moore, and D. A. Paige (2008), The formation of Tharsis on Mars: What the line-of-sight gravity is telling us, *J. Geophys. Res.*, *113*, E10011, doi:10.1029/2007JE003050.

Wolff, M. (1969), Direct measurements of the Earth's gravitational potential using a satellite pair, *J. Geophys. Res.*, *74*, 5295–5300.

Zuber, M. T., et al. (2013a), Gravity field of the Moon from the Gravity Recovery and Interior Laboratory (GRAIL) mission, *Science*, *339*, 668–671, doi:10.1126/science.1231507.

Zuber, M. T., D. E. Smith, D. H. Lehman, T. L. Hoffman, S. W. Asmar, and M. M. Watkins (2013b), Gravity Recovery and Interior Laboratory (GRAIL): Mapping the Lunar Interior from Crust to Core, *Space Sci. Rev.*, Published online, 04 Jan 2013, *178*, 3–24, doi:10.1007/s11214-012-9952-7